Chapter 34

CONTROL OF SINGLE DROP COMBUSTION AND EMISSION BY MEANS OF EMULSIFYING FUEL WITH WATER

S. M. Frolov, V. S. Posvyanskii, V. Ya. Basevich, A. A. Belyaev,
O. Esmilaire, C. Jablon, and P. Schmelzle

The mathematical model of emulsion-fuel drop combustion has been suggested and implemented for comparing combustion and pollutant emission performance of pure-fuel and emulsified-fuel drops. The model has been validated against available experimental data for combustion of pure-hydrocarbon fuel drops under low-gravity and normal gravity conditions. It has been shown that addition of water in the amount higher than 4%–5% (wt.) to a hydrocarbon fuel allows one to considerably improve pollutant emission performance of fuel in terms of soot, CO and NO emission. The findings were found to be in qualitative agreement with experimental data on emulsified fuel (Aquazol) combustion in Direct Injection Diesel engines.

34.1 INTRODUCTION

Chemical and physical processes accompanying combustion of a single fuel drop are complex and interrelated. Chemical processes include oxidation reactions of fuel and its decomposition products, reactions of NOx and soot formation, etc. Physical processes encounter transient molecular and convective heat and mass transfer and viscous dissipation in liquid and gas phases, phase transition, radiation, drop thermal expansion, deformation and breakup, microexplosion of a multicomponent (solution or emulsion) drop, etc. Particular issues are flame ignition and extinction phenomena.

Experimentally, ignition and combustion of fuel–water emulsion drops has been studied elsewhere (see, for example, [1–11]). No considerable chemical effect of water on combustion processes was detected, though the efficiency of energy

transfer in triple collisions with water molecules is known to be quite high. Also, water is known to be a catalyst of combustion in oxidative environment, provided hydrogen is absent (e.g., in a dry mixture of carbon monoxide with oxygen). During oxidation of hydrocarbons, water is one of main combustion products and is not a deficient species. It is commonly accepted that the governing mechanism of the effect of water on the combustion process and on the formation of various combustion products is most probably the reduction of temperature with increase of water content in the reactive mixture. In particular, this effect is responsible for reduction of NOx with water addition.

Under certain conditions, combustion of emulsion drops is known to exhibit disruption ('microexplosion'). Drop microexplosion may occur when the temperature of steam bubble nucleation in emulsion is lower than the hydrocarbon boiling temperature. According to [8], there always exists a delay time between the ignition and microexplosion of fuel–water emulsion drops. This delay time is determined by the time necessary to superheat the interior of the drop to the required nucleation temperature. The required degree of superheat to initiate boiling of water within the emulsified drop is a function of the physical properties of fuel. Consequently, different delay times are observed for different water contents in fuel emulsions. Water concentration in the emulsion was shown to have a weak effect on the drop mass loss during the period from drop ignition to microexplosion.

Experimental results on combustion of unsupported single drop of Diesel fuel and its emulsions with water are presented by Gollahalli *et al.* [7]. The experiments covered the following range of variables: volume fraction of water (0–0.3), surfactant concentration (0–0.05), injection temperature (298–380 K), chamber temperature (400–950 K), chamber pressure (0.44–3.92 MPa), chamber inlet oxygen concentration (0.16–0.75). The initial diameter of emulsion drops was 1600 μm. The mean diameter of water drops in emulsion was 2 μm. The results show that the drop of emulsified fuel undergo microexplosion during combustion. Drop fragmentation increases with water content, surfactant content, injection temperature, chamber oxygen concentration, and chamber temperature, but is not significantly dependent on chamber pressure. At low water contents, a small tendency to microexplosion was observed. The emulsion drops were more difficult to ignite than pure-fuel drops, they had shorter flames in the wake than pure-fuel drops, their flames were light yellow in color, had ragged edges, exhibited sudden changes in width and length, and split into multiple paths. The flame temperature, exhaust emissions of NOx were found to be complexly dependent upon the variables examined.

Contrary to pure-fuel drops, nowadays no satisfactory quantitative theory exists for combustion of emulsified-fuel drops. A simple quasi-steady mathematical model of the process was proposed by Law [12] that does not take into account drop heating, fuel vapor accumulation processes, and gas-phase kinetics. Nevertheless, the model provides some physical grounds for understanding the effect

of water addition to hydrocarbon fuel on the reduction of pollutant formation and drop microexplosion. A mathematical model describing the growth of an internal vapor bubble produced by homogeneous nucleation within a liquid drop was proposed by Shusser & Weihs [13] that takes into account the instability of the liquid–vapor interface.

The ultimate objective of the research summarized in this paper is to compare combustion and pollutant-emission performances of pure-fuel and emulsified-fuel drops. Based on general thermodynamic considerations, it is anticipated that addition of a volatile liquid component (e.g., water) to a heavy hydrocarbon fuel in emulsified form allows one to control drop combustion by decreasing the amount of fuel vapor accumulated between the flame and the drop surface and displacing the flame closer to the surface. As a consequence, more intense interphase fluxes can occur, affecting drop lifetime and pollutant emission. Recently [14], it has been demonstrated that the use of a specially prepared diesel fuel – water emulsion (Aquazole) in heavy-duty Diesel engines provided a significant decrease in smoke as well as some reduction in CO and NOx emission in engine exhaust gases. The mathematical model described herein is aimed at a better understanding of the encountered phenomena.

34.2 MODEL FORMULATION

34.2.1 Statement and Main Assumptions

The objective of the research is to compare combustion and pollutant-emission performances of pure-fuel and emulsified-fuel drops under low-gravity conditions. A pure-fuel drop is a drop of a heavy primary hydrocarbon. The emulsion drop comprises of the continuous phase (fuel) and dispersed phase (volatile liquid component — water). At any time, water is uniformly distributed in the drop in the form of fine droplets. From now on, the latter will be referred to as microdrops, whereas the drop itself will be referred to as a mother or emulsion drop. Emulsion drop heating results in internal evaporation of water and formation of steam bubbles around microdrops. Thus, in general, the emulsion drop consists of three phases: 1 — fuel, 2 — microdrops, and 3 — bubbles. With no volatile liquid component, the emulsion drop is equivalent to the pure-fuel drop.

For modeling the gasification and combustion of the pure-fuel and emulsion drop, the following simplifying assumptions are adopted:

(1) the mother drop has a spherical shape;

(2) no dissolution of water in fuel occurs;

(3) forced convection and buoyancy effects in the gas phase are not considered;

(4) water loading ratio is assumed small and constant in time and space; microdrops are initially monodispersed;

(5) gas-phase pressure is constant;

(6) microdrops and bubbles are spherical and do not coagulate or break up;

(7) Laplace pressure for the mother drop is negligible;

(8) fuel has a considerably lower vapor pressure than water;

(9) drop history is continuous, i.e., no instabilities are considered leading to abrupt violation of drop integrity (microexplosion);

(10) microdrops and bubbles attached to them, when coexisting, heat up uniformly and have the same temperature;

(11) radiation heat transfer is neglected;

(12) approximation of independent diffusion of gaseous species is considered; and

(13) concentration of fuel vapor at the emulsion drop surface is governed by the equilibrium relationship.

All the assumptions are discussed in the following sections.

34.2.2 Governing Equations

At any time t, the mother drop occupies the region $0 < r < r_s(t)$. The drop surface coordinate r_s varies in time due to evaporation of continuous phase and due to phase transition of water in drop interior and thermal expansion of steam bubbles. Thus, the rate of surface motion, u_s, is a function of time and does not depend on radial coordinate:

$$u_s = u_s(t)$$

The consequence of assumptions (1) to (4) is that no internal diffusion of species and convection exists inside the mother drop and one can always distinguish between phases $i = 1$, 2, and 3. Each of the three phases in the emulsion drop has its own temperature $T_{li}(r,t)$, density $\rho_{li}(r,t)$, specific heat $c_{li}(r,t)$, and thermal conductivity $\lambda_{li}(r,t)$. The density of three-phase medium in the drop is defined as:

$$\rho_{l\Sigma}(r,t) = \sum_{i=1}^{3} \varphi_i(r,t)\rho_{li}(r,t)$$

where $\varphi_i(r,t)$ is the volume fraction of the ith phase. The volume fractions of phases are related to each other by the formula:

$$\varphi_1(r,t) + \varphi_2(r,t) + \varphi_3(r,t) = 1 \tag{34.1}$$

The mass fraction of water (including steam) in the emulsion drop is represented by water loading ratio, η. To satisfy assumption (4), the following constraints on the densities of liquid fuel and water in the emulsion drop should be imposed:

$$\rho_{l1}(r,t) = const = \rho_{l1}^0 \tag{34.2}$$

$$\rho_{l2}(r,t) = const = \rho_{l2}^0 \tag{34.3}$$

where upper index 0 denotes the initial value. Assumption (4) allows one to write an additional expression between φ_i and ρ_{li}:

$$\eta \sum_{i=1}^{3} \varphi_i(r,t)\rho_{li}(r,t) = \varphi_2(r,t)\rho_{l2}^0 + \varphi_3(r,t)\rho_{l3}(r,t) \tag{34.4}$$

Contrary to the densities of liquid phases, the density of steam, ρ_{l3}, is taken variable. It is calculated by using the ideal-gas equation of state and the effect of Laplace pressure:

$$p_g + \frac{2\sigma_{l1}}{r_3} + \frac{2\sigma_{l1}}{r_s} \approx \frac{\rho_{l3} R T_{l3}}{G_{l3}} \tag{34.5}$$

where p_g is the gas-phase pressure assumed constant (assumption (5)), i.e., $p_g = p_g^0$, σ_{l1} is the coefficient of surface tension of fuel, $r_3(r,t)$ is the spherical bubble radius that satisfies the constraint $r_3(r,t) \geq r_2(r,t)$, r_2 is the spherical microdrop radius (assumption (6)), $G_{l3} = G_{l2}$ is the molecular mass of water, $T_{l3} = T_{l3}(r,t)$ is the bubble temperature, R is the universal gas constant. The third term in the left-hand side (LHS) of Eq. (34.5) is neglected according to assumption (7), as the mother drop size is typically much larger than the microdrop size. In addition, Eq. (34.5) implies that evaporation of fuel into steam bubbles is absent (assumption (8)). At small sizes of microdrops and bubbles, Laplace pressure can result in a considerable water overheat [15].

According to assumption (9), the evolution of the emulsion drop is continuous and, thus, can be considered in terms of differential equations. The radius of the emulsion drop, $r_s(t)$, is governed by the following balance equation:

$$\frac{dM}{dt} = 4\pi r_s^2 \rho_{l\Sigma}\Big|_{r=r_s} u_s$$

where M is the drop mass given by the formula:

$$M = 4\pi \int_0^{r_s(t)} r^2 \rho_{l\Sigma}(r)\, dr$$

The total energy of the unit volume of the ith phase is equal to $\varphi_i \rho_{li} I_{li}$, where $I_{li} = I_{li}(r,t)$ is the enthalpy of the ith phase. The energy of the continuous phase 1 varies due to heat flux to the mother drop interior $q = q(r,t)$ and due to interphase heat fluxes from the continuous phase to water and steam, denoted as $Q_{12} = Q_{12}(r,t)$ and $Q_{13} = Q_{13}(r,t)$, respectively. Note that heat flux q is not equal to the external heat flux to the mother drop, because a part of drop energy goes on phase transition at the drop surface (see Eq. (34.23) below). The energy of phase 2 varies due to heat flux Q_{12} and water-to-steam phase transition. The energy required for the phase transition is assumed to be extracted from phase 2 as this phase has a larger coefficient of thermal conductivity as compared to phase 3. The extracted energy is thus equal to $M_{23}(I_{l2} + H_{l2})$, where $M_{23} = M_{23}(r,t)$ is the rate of water microdrop evaporation per unit volume and H_{l2} is the latent heat of evaporation. The energy of phase 3 varies due to heat flux Q_{13} and due to addition of energy $M_{23}(I_{l2} + H_{l2})$ caused by water-to-steam phase transition. Thus, the equations governing heat evolution in the emulsion drop are as follows:

$$\frac{\partial}{\partial t}\left(\varphi_l \rho_{l1} I_{l1}\right) = q - Q_{12} - Q_{13} \tag{34.6}$$

$$\frac{\partial}{\partial t}\left(\varphi_2 \rho_{l2} I_{l2}\right) = Q_{12} - M_{23}(I_2 + H_{l2}) \tag{34.7}$$

$$\frac{\partial}{\partial t}\left(\varphi_3 \rho_{l3} I_{l3}\right) = Q_{13} + M_{23}(I_2 + H_{l2}) \tag{34.8}$$

The term M_{23} is defined as:

$$\frac{\partial \varphi_2 \rho_{l2}}{\partial t} = -M_{23} \tag{34.9}$$

The right-hand side (RHS) of Eq. (34.7) can be treated as follows: a part of flux Q_{12} is consumed for microdrops heating and the other part is consumed to water-to-steam phase transition. To simplify the problem statement, a coefficient $\nu = \nu(r,t)$ is introduced that denotes a fraction of heat flux, Q_{12}, absorbed by the water-to-steam phase transition, i.e.:

$$M_{23} = M_{23}(r,t) = \frac{\nu Q_{12}}{H_{l2}} \tag{34.10}$$

Coefficient ν allows one to smoothen the transition between the transient and quasi-steady evaporation of microdrops and is a result of omitting the detailed consideration of microdrop heating and evaporation (assumption (10)).

The enthalpies of phases satisfy the following thermodynamic relations:

$$dI_{l1} = c_{l1} dT_{l1}\,, \quad dI_{l2} = c_{l2} dT_{l2}\,, \quad dI_{l3} \approx c_{l3} dT_{l3} \tag{34.11}$$

with the last relationship valid at pressure considerably below the critical pressure [16] when

$$\left(\frac{\partial H_{l2}}{dT}\right)^s \ll c_{l3}$$

(the upper index s relates to phase equilibrium).

Term q in the RHS of Eq. (34.6) is equal to

$$q = \frac{1}{r^2}\frac{\partial}{\partial r}\left(\lambda_{l1} r^2 \frac{\partial T_{l1}}{\partial r}\right) \tag{34.12}$$

With regard for Eqs. (34.3) and (34.10) to (34.12), Eqs. (34.6) to (34.9) take the form:

$$c_{l1}\varphi_1\rho_{l1}\frac{\partial T_{l1}}{\partial t} = \frac{1}{r^2}\frac{\partial}{\partial r}\left(\lambda_{l1} r^2 \frac{\partial T_{l1}}{\partial r}\right) - Q_{12} - Q_{13} \tag{34.13}$$

$$c_{l2}\varphi_2\rho_{l2}\frac{\partial T_{l2}}{\partial t} = (1-\nu)Q_{12} \tag{34.14}$$

$$c_{l3}\varphi_3\rho_{l3}\frac{\partial T_{l3}}{\partial t} = Q_{13} \tag{34.15}$$

$$\rho_{l2}\frac{\partial \varphi_2}{\partial t} = -\frac{\nu Q_{12}}{H_{l2}} \tag{34.16}$$

Note that under conditions close to equilibrium of phases 2 and 3, the term

$$-\frac{\nu Q_{12}}{H_{l2}}\left(I_{l3} - I_{l2} - H_{l2}\right)$$

arising in RHS of Eq. (34.15) after transformation of Eqs. (34.6) to (34.9) vanishes as

$$I_{l2} = I^s_{l2} + c_{l2}\left(T_{l2} - T^s_{l2}\right)$$
$$I_{l3} = I^s_{l2} + H_{l2} + c_{l3}\left(T_{l3} - T^s_{l2}\right)$$

and at $T_{l2} \to T^s_{l2}$ and $T_{l3} \to T^s_{l2}$ (valid at $M_{23} \neq 0$) one arrives at condition $I_{l3} \approx I_{l2} + H_{l2}$.

Terms Q_{12} and Q_{13} in the RHS of Eqs. (34.13) to (34.16) are given by the following relationships:

$$Q_{12} = \alpha_{12} S_2 (T_{l1} - T_{l2})$$
$$Q_{13} = \alpha_{13} S_3 (T_{l1} - T_{l3})$$

where $\alpha_{12}(r,t)$ and $\alpha_{l3}(r,t)$ are the heat exchange coefficients between fuel and microdrops and between fuel and bubbles, respectively, and $S_2(r,t)$ and $S_3(r,t)$

are the specific surface areas of microdrops and bubbles, respectively. Coefficients α_{12} and α_{13} are calculated by using the formulae:

$$\alpha_{12} = \frac{\mathrm{Nu}\lambda_{l1}\delta}{2r_2} = \frac{\lambda_{l1}\delta}{r_2}$$
$$\alpha_{13} = \frac{\mathrm{Nu}\lambda_{l3}(1-\delta)}{2r_3} = \frac{\lambda_{l3}(1-\delta)}{r_3}$$

where $\mathrm{Nu} = 2$ is the characteristic Nusselt number, and parameter δ is introduced to properly distribute the heat flux from the continuous phase to the dispersed phases.

In order to determine variables S_2, S_3, r_2, and r_3, it is worth to introduce the number density of microdrops, n_2, that is constant in time and space (as follows from assumptions (4) and (6)):

$$n_2 = n_2^0 = \frac{\eta\rho_{l\Sigma}^0}{(4\pi/3)(r_2^0)^3\rho_{l2}^0}$$

where the initial radius of microdrop, r_2^0, is a preset parameter of the problem (see assumption (4)). The specific surface areas of microdrops and bubbles are then given by

$$S_2 = 4\pi r_2^2 n_2$$
$$S_3 = 4\pi r_3^2 n_2$$

Since the volume of a single microdrop is $(4\pi/3)r_2^3$, its radius is readily obtained from the formula:

$$r_2(r,t) = \left(\frac{3}{4\pi n_2}\,\varphi_2(r,t)\right)^{1/3}$$

Similarly, the radius of a bubble is found as:

$$r_3(r,t) = \left[\frac{3}{4\pi n_2}\,(\varphi_2(r,t) + \varphi_3(r,t))\right]^{1/3}$$

Now, turn over to the determination of coefficients ν and δ entering Eqs. (34.13) to (34.16).

Coefficient δ partitions the heat flux to dispersed phases into two fluxes: Q_{12} and Q_{13}. At low temperatures, when T_{l2} (and T_{l3}, assumption (10)) are considerably less than the characteristic boiling temperature of water, most of heat is absorbed by microdrops. At temperatures T_{l2} (and T_{l3}) close to the boiling temperature, most of heat is absorbed by bubbles. The characteristic boiling temperature T_{b2} is relevant to water pressure, p, in microdrops determined as

$$p \approx p_g + \frac{2\sigma_{l2}}{r_2} + \frac{2\sigma_{l1}}{r_3} + \frac{2\sigma_{l1}}{r_s}$$

where σ_{l2} is the coefficient of surface tension of water. According to assumption (7), $r_s \gg r_3(r,t) \geq r_2(r,t)$ and the last term in the RHS of the above equation can be neglected. In view of it, coefficient δ is modeled as

$$\delta = \begin{cases} 1 & \text{at } \xi < 0 \\ -2(1-\xi)^3 + 3(1-\xi)^2 & \text{at } 0 \leq \xi \leq 1 \\ 0 & \text{at } \xi > 1 \end{cases}$$

where ξ is defined as

$$\xi = \frac{T_{l2} - T_{l2}^0}{T_{b2} - T_{l2}^0} = \frac{T_{l3} - T_{l2}^0}{T_{b2} - T_{l2}^0}$$

When microdrops attain the minimum preset size $r_2^{\min}$, coefficient δ and, hence, heat flux Q_{12} tend to zero. Since then, only heat flux Q_{13} is nonzero that results in thermal expansion of bubbles. Note that $r_2^{\min}$ has to be introduced to avoid singularities.

Consider coefficient ν. At transient evaporation of microdrops, a fraction of heat flux, Q_{12}, absorbed by the water-to-steam phase transition, is in general a function of microdrop temperature T_{l2}. At quasi-steady evaporation of microdrops, when they are heated to nearly the boiling temperature, coefficient ν is zero. For simplicity, it is assumed that ν is a preset function of the dimensionless temperature ξ:

$$\nu = \begin{cases} \nu_0 & \text{at } \xi < 0 \\ 2(\nu_0 - 1)\xi^3 - 3(\nu_0 - 1)\xi^2 + \nu_0 & \text{at } 0 \leq \xi \leq 1 \\ 1 & \text{at } \xi > 1 \end{cases}$$

where $0 \leq \nu_0 \leq 1$ is the problem parameter (constant).

In region $r_s < r < \infty$, occupied by the gas phase, the continuity equation and the equation of thermal conductivity for the mixture and the continuity equation for gas-phase species $j = 1, 2, \ldots, N$ have the standard form without radiation heat loss (assumption (11)):

$$\frac{\partial \rho_g}{\partial t} = -\frac{1}{r^2}\frac{\partial}{\partial r}\left(r^2 \rho_g u_g\right) \tag{34.17}$$

$$c_g \rho_g \frac{\partial T_g}{\partial t} = \frac{1}{r^2}\frac{\partial}{\partial r}\left(\lambda_g r^2 \frac{\partial T_g}{\partial r}\right) - c_{pg}\rho_g u_g \frac{\partial T_g}{\partial r} + \Phi \tag{34.18}$$

$$\rho_g \frac{\partial Y_{gj}}{\partial t} = \frac{1}{r^2}\frac{\partial}{\partial r}\left(\rho_g D_{gj} r^2 \frac{\partial Y_{gj}}{\partial r}\right) - \rho_g u_g \frac{\partial Y_{gj}}{\partial r} + w_{gj} \tag{34.19}$$

The terms in Eqs. (34.18) and (34.19), reflecting the effect of chemical reaction in the gas phase, are:

$$\Phi = \sum_{k=1}^{L} H_k A_k T_g^{n_k} \exp\left(-\frac{E_k}{RT_g}\right) \prod_{j=1}^{N} \left(\frac{Y_{gj}\rho_g}{G_{gj}}\right)^{\nu'_{j,k}}$$

$$\omega_{gj} = G_{gj} \sum_{k=1}^{L} \left(\nu''_{j,k} - \nu''_{j,k}\right) A_k T_g^{n_k} \exp\left(-\frac{E_k}{RT_g}\right) \prod_{j=1}^{N} \left(\frac{Y_{gj}\rho_g}{G_{gj}}\right)^{\nu'_{j,k}}$$

The gaseous mixture obeys the Redlich–Kwong real-gas equation of state (see [16]):

$$p_g = R\frac{T_g}{\nu_g}\left[\frac{\nu_g}{\nu_g - b_g} - \frac{\Omega_a}{\Omega_b}\frac{b_g}{\nu_g - b_g}F_g\right] \tag{34.20}$$

where $\nu_g = G_g/\rho_g$ is the molar volume of gaseous mixture, G_g is the mean molecular mass

$$G_g = \left[\sum_j \frac{Y_{gj}}{G_{gj}}\right]^{-1}$$

and other terms determined as

$$b_g = G_g \sum_j \frac{Y_{jg}}{G_{gj}} b_j\,, \quad b_j = 82.04\,\frac{\Omega_b T_{cj}}{p_{cj}}\,,\ j = 1, 2, \ldots, N$$

$$F_g = \frac{\left(\sum_j \left(Y_{gj}/G_{gj}\right)\left(T_{cj}/(Q_j^{1.5}p_{cj})\right)^{1/2}\right)^2}{\sum_j (Y_{gj}/G_{gj})(T_{cj}/p_{cj})}\,, \quad \theta_j = \frac{T_g}{T_{cj}}$$

$$\Omega_a = 0.4275, \quad \Omega_b = 0.0866$$

where T_{cj} and p_{cj} are the critical temperature (in K) and pressure (in bar) of the jth species, respectively.

Thus, the list of problem variables includes: u_s, φ_1, φ_2, φ_3, ρ_{l1}, ρ_{l2}, ρ_{l3}, T_{l1}, T_{l2}, T_{l3}, u_g, ρ_g, T_g, and Y_{gj} $(j = 1, 2, \ldots, N)$, i.e., $13 + N$ variables. These variables enter $12 + N$ equations: (34.1)–(34.5), (34.13)–(34.18), $N \times$ (34.19), and (34.20). The additional equation for the unknown variable u_s (problem eigenvalue) comes from the constraint (34.27) below and conditions tailoring of the solutions at the interface between gas and liquid (Eqs. (34.21) to (34.26) below). These conditions are discussed in section 34.2.4.

The list of physical properties to be specified contains liquid-phase properties λ_{l1}, λ_{l2}, λ_{l3}, c_{l1}, c_{l2}, c_{l3}, H_{l1}, H_{l2}, σ_{l1}, and σ_{l2}, and gas-phase properties: c_{gj}, D_{gj}, λ_{gj} $(j = 1, 2, \ldots, N)$ as well as molecular masses and critical parameters of all species encountered: G_{li} $(i = 1, 2, 3)$, G_{gj} $(j \neq i)$, T_{cj}, and p_{cj} $(j = 1, 2, \ldots, N)$. List of problem parameters includes: η, p_g, r_s^0, r_2^0, $r_2^{\min}$, and thermochemical parameters of reactions H_k, A_k, E_k, n_k, $\nu'_{i,k}$ $(k = 1, 2, \ldots, L;\ i = 1, 2, \ldots, N)$.

Table 34.1 Key parameters of species used in calculations

Substance	Parameter								
	ω	T_c K	p_c bar	σ A	ε/k K^{-1}	H_b cal/mol	T_b K	$\alpha \times 10^6$ K	A
C_7H_{16}	0.351	540.2	27.0	6.310	459.7	7576	371.6	2.40418	9.5566
$C_{10}H_{22}$	0.490	617.6	20.8	7.160	540.1	9388	447.3	1.83310	10.1789
$C_{14}H_{30}$	0.679	694.0	16.0	8.020	626.5	11380	526.7	1.32760	10.8801
H_2O	0.344	647.3	217.6	2.641	809.1	9717	373.2	0.34679	12.4575
O_2	0.021	154.6	49.8	3.467	106.7	—	90.2	—	—
N_2	0.040	126.2	33.5	3.798	71.4	—	77.4	—	—
CO_2	0.225	304.2	72.8	3.941	195.2	—	194.7	—	—
CO	0.049	132.9	34.5	3.690	91.7	—	81.7	—	—
H_2	0.010	33.2	12.8	2.827	59.7	—	20.4	—	—
NO	0.607	180.0	64.0	3.492	116.7	—	121.4	—	—

34.2.3 Liquid and Gas Properties

Thermophysical properties of individual substances and their mixtures were calculated by using recommendations of [16]. Table 34.1 presents a list of key parameters entering the correlations used. Here, ω is the Pitz factor, σ and ε are the parameters of Lenard–Jones potential, k is the Boltzmann constant, and α and A are the parameters entering the phase equilibrium Eq. (34.27).

34.2.4 Boundary Conditions

The temperature distribution inside the drop is symmetric, i.e.:

$$r = 0\,, \quad \frac{\partial T_{l1}}{\partial r} = 0 \tag{34.21}$$

At the drop surface, $r = r_s$, the continuity of temperature profile and the balance of heat fluxes should hold, as well as the balance of mass and continuity of species, and the condition of equilibrium evaporation. The first of the mentioned conditions can be written as:

$$r = r_s\,, \quad T_{l1} = T_g \tag{34.22}$$

The condition of heat balance is:

$$r = r_s\,, \quad \lambda_{l1} = \frac{\partial T_{l1}}{\partial r} - \frac{\rho_{l\Sigma}\, u_s H_{l1}}{G_{l1}} = \lambda_g \frac{\partial T_g}{\partial r} \tag{34.23}$$

Conservation of mass at the drop surface is given by:

$$r = r_s\,, \quad -\rho_{l1}\, u_s = \rho_g \left(u_g - \frac{dr_s}{dt} \right) \tag{34.24}$$

Note that dr_s/dt is in general not equal to u_s due to a possibility of drop thermal expansion.

The balance of mass for all chemical species $j = 1, 2, \ldots, N$ is taken in the form:

$$r = r_s\,, \quad \rho_g D_{gj} \frac{\partial Y_{gj}}{\partial r} - \rho_g \left(u_g - \frac{dr_s}{dt} \right) Y_{gj} = \rho_{l\Sigma}\, u_s\, \beta \tag{34.25}$$

where β is the coefficient that is nonzero for fuel and water and zero for other species. In order to apply Eq. (34.25), one has to know the values of parameter β for fuel and water. Assumptions (2) and (4) of section 34.2.1 make it reasonable to write:

$$\begin{aligned} &\beta = 1 - \eta \quad && \text{for fuel} \\ &\beta = \eta && \text{for water} \\ &\beta = 0 && \text{for other species} \end{aligned}$$

Clearly, such a definition of β is consistent with the requirement of elementary balance between liquid- and gas-phase species without solving the diffusion equation in the liquid phase.

Finally, it is natural to assume that at a large distance $r = L_\infty$ from the drop–gas interface, heat and mass fluxes vanish:

$$r = L_\infty\,, \quad \frac{\partial T_g}{\partial r} = 0\,, \quad \frac{\partial Y_{gj}}{\partial r} = 0 \tag{34.26}$$

Boundary conditions (34.21) to (34.26) provide the solution of the governing equations once the velocity u_s is preset. To determine the eigenvalue of u_s, one has to supplement the set of governing equations with an additional constraint. One of possibilities is to specify the equilibrium fuel vapor concentration at the drop surface. As fuel is considered to form a continuous phase in the emulsion drop and water loading ratio is small (assumption (4)), it is assumed that fuel vapor concentration, $Y^s_{g,\mathrm{Fu}}$, at the drop surface is given by the equilibrium relationship (assumption (13)):

$$r = r_s\,, \quad Y^s_{g,\mathrm{Fu}} = \frac{p^s_{g,\mathrm{Fu}}}{p_g} \frac{G_{g,\mathrm{Fu}}}{G_g}$$

where vapor pressure $p^s_{g,\mathrm{Fu}}$ (bar) is calculated by using the formula [17]:

$$p^s_{g,\mathrm{Fu}} = \left[\left(\frac{T_s}{\alpha_{\mathrm{Fu}}} \right)^{1/8} - A_{\mathrm{Fu}} \right]^8 \tag{34.27}$$

where T_s is the drop surface temperature, and α_{Fu} and A_{Fu} are the constants presented in Table 34.1 as α and A.

34.2.5 Initial Conditions

Initial conditions at $t = 0$ are given by:

$$M = M^0 \quad (r_s = r_s^0)$$

$$\begin{aligned} &r < r_s^0: \ \varphi_i = \varphi_i^0\,, \quad \rho_{li} = \rho_{li}^0\,, \quad T_{li} = T_{li}^0\,; \quad i = 1,2,3 \\ &r > r_s^0: \ T_g = T_g^0(r)\,, \quad Y_{gj} = Y_{gj}^0(r)\,, \quad j = 1,2,\ldots,N \\ &r = r_s: \ T_{l1}^{s\,0} = T_g^{s\,0}\,, \quad Y_{g,\mathrm{Fu}}^s = Y_{g,\mathrm{Fu}}^{s\,0}\,, \quad Y_{g,\mathrm{H_2O}}^s = Y_{g,\mathrm{H_2O}}^{s\,0} \end{aligned} \tag{34.28}$$

Initial distribution of gas density $\rho_g^0(r)$ is found from Eq. (34.20) and initial distributions $T_g^0(r)$ and $Y_{gj}^0(r)$. Initial values φ_i^0 are calculated based on η, ρ_{l1}^0, ρ_{l2}^0, and the initial values of microdrop and bubble radii $r_2 = r_2^0$ and $r_3 = r_3^0 = r_2^0$.

Note that the governing equations of section 34.2.2 do not contain time derivatives of u_g. In view of it, the field of velocity u_g follows 'immediately' the field of gas density ρ_g. In the computational scheme, this allows one to rewrite Eq. (34.17) for u_g so that it does not contain time derivatives of other variables. This is achieved by differentiating the equation of state (34.20) with respect to time and using Eqs. (34.18), (34.19), and condition $dp/dt = 0$.

34.2.6 Problem Parameters

Problem parameters η, p_g, r_s^0, r_2^0, $r_{2,\min}$, and L_∞ vary within the following ranges: $0 \le \eta \le 0.2$, $p_g = 1$ bar, $10 \le r_s^0 \le 2000$ μm, $0.3 \le r_2^0 \le 1.0$ μm, $r_{2,\min} = 0.1$ μm, $L_\infty = (100\text{–}200) r_s^0$, and $\nu = 0.5$.

Gas-phase oxidation of heavy hydrocarbon fuels (n-alkanes, $\mathrm{C}_n\mathrm{H}_{2n+2}$) is modeled by the overall reaction mechanism of Table 34.2 containing 8 forward and 2 reverse reactions ($L = 10$) and 9 species ($N = 9$): $\mathrm{C}_n\mathrm{H}_{2n+2}$, O_2, N_2, CO, CO_2, H_2, $\mathrm{H}_2\mathrm{O}$, NO, and So (soot). Thermochemical parameters of reactions: H_k, A_k, E_k, and n_k ($k = 1,2,\ldots,L$) are also listed in Table 34.2. In addition, it is shown also the values of preexponential factors of NO and soot formation reactions No. 5 and No. 7. In the mechanism of Table 34.2, soot is considered as an equivalent gas with the molecular mass $G_{\mathrm{so}} = 12$ and binary diffusion coefficient taken constant and small (equal to 0.01 cm^2/s). As the amount of soot is usually relatively small, all other properties of soot particles were taken equal to those of diluent (nitrogen). The kinetic mechanism of Table 34.2 has been preliminarily validated for laminar premixed [18, 19] and laminar diffusion counterflow flames [20]. Evlampiev *et al.* [20] have validated a simple soot formation mechanism (reactions No. 7 and No. 8 in Table 34.2) against experimental data for premixed methane–oxygen flames reported by Xu *et al.* [21].

Table 34.2 Overall mechanisms of fuel oxidation

Reaction	H, $\frac{\text{kcal}}{\text{mol}}$	Forward A, mol, l, s	Forward n	Forward E, $\frac{\text{kcal}}{\text{mol}}$	Reverse A, mol, l, s	Reverse n	Reverse E, $\frac{\text{kcal}}{\text{mol}}$
1. $C_nH_{2n+2} + (n+0.5)O_2 = nCO + (n+1)H_2O$	125	$7 \cdot 10^{14}/p$	0.0	50.0			
2. $H_2 + H_2 + O_2 = H_2O + H_2O$	114	$7.0 \cdot 10^{13}/p^{0.5}$	0.0	21.0			
3. $CO + CO + O_2 = CO_2 + CO_2$	134	$8.5 \cdot 10^{12}/p^{1.5}$	0.0	21.0			
4. $CO + H_2O = CO_2 + H_2$	10	$1.0 \cdot 10^{12}/p$	0.0	41.5	$3.1 \cdot 10^{13}/p$	0.0	49.1
5. $C_nH_{2n+2} + O_2 + N_2 = C_nH_{2n+2} + NO + NO$	−43	A_5/p^2	0.0	50.0			
6. $O_2 + N_2 = NO + NO$	−43	$1.7 \cdot 10^{17}$	−0.5	136.0	$4.1 \cdot 10^{15}$	−0.5	93.3
7. $C_nH_m + C_nH_m = 2nSo^* + mH_2$	$-h_7$	A_7/p	0.0	50.0			
8. $So + So + O_2 = CO + CO$	394	$7 \cdot 10^{14}/p$	0.0	0.0			

*So denotes soot.

Parameters of NO and soot formation reactions Nos. 5 and 7

n	A_5, 10^{14} l/mol·s	A_7, 10^{14} l/mol·s	h_7, kcal/mol
7	2.02	0.040	2430
10	3.10	0.229	3450
14	4.10	2.550	4826

34.2.7 Solution Procedure

For integrating the set of governing equations, the implicit finite difference scheme was applied. Since the problem is nonlinear, the solution procedure included iterations at each time step. During the iteration cycle, first, variables ρ_{li}, u_s, T_{li}, ρ_g, u_g, T_g, and $Y_{g,\text{Fu}}$ were calculated as a result of joint solution of the corresponding equations, and then the other variables (Y_{gj}, $j \neq$ Fu) were determined on their basis. The iterations were terminated after a convergence criterion was met. The integration time step was chosen automatically, depending on the convergence behavior.

The important point of the algorithm is the linearization of the conditions at the drop interface. To ensure rapid convergence of the iterations, the full Newton-type linearization of the interface conditions was required.

The problem under consideration contains different temporal and spatial scales. In particular, the mother drop, microdrop, and bubble sizes are usually

much smaller than the characteristic dimension of the gas volume involved in the physical and chemical processes outside the drop. In view of it, the finite difference grid had variable grid node spacing. Since the processes at the drop interface determine the solution, the grid nodes were usually clustered near the interface.

The computational grid applied in this study consisted of three sections: (D): drop ($n_D + 1$ nodes); (M): adjacent gas (n_M nodes); and (A): ambient gas (n_A nodes).

Node n_D corresponds to the liquid–gas interface. The total number of grid nodes, $n_G = n_D + n_M + n_A + 1$ remained constant during the whole run.

Denote the spatial step between two successive nodes as $\Delta r_k = r_k - r_{k-1}$, where $0 \le k \le n_G$ is the node number. The spatial distributions of grid nodes in the above sections at any time step are governed by the progression coefficients P_D and P_M that are the preset values. If the progression coefficients equal to unity, the computational grid in sections (D) and (M) is uniform with the constant spatial step $\Delta r = r_s/n_D$. The progression coefficient $P_D < 1.0$ allows one to compress the grid towards the liquid–gas interface to obtain the spatial step distribution: $\Delta r_k = h_1 P_D^{k-1}$ with $h_1 = r_s/\Sigma_{k=0}^{n_D-1} P_D^k$. The progression coefficient P_M can be used to compress ($P_M < 1.0$) or expand ($P_M > 1.0$) the grid in the adjacent gas section as $\Delta r_{n_D+k} = (\Delta r_{n_D}) P_M^{k-1}$ (at $1 \le k \le n_M$). Node coordinate distribution in section (A) is taken in the form $r_k = r_M + (L_\infty - r_M) f(\psi_k)$, $1 < k \le n_A$, where $r_{n_D+n_M} = (\Delta r_{n_D}) P_M^{n_M-1}$, $f(\psi_k) = \mathrm{sh}(\tau\psi_k)/\mathrm{sh}(\tau)$, $\psi_k = k/n_A$, and the value of τ is found from solving the transcendental equation

$$\frac{h_M}{L_\infty - r_M} = \frac{\mathrm{sh}(\tau/n_A)}{\mathrm{sh}(\tau)}$$

with $h_M = r_{n_D+n_M} - r_{n_D+n_M-1}$.

All grid nodes, except for the node at $r = 0$, were moving with time due to variation of the droplet size. Each kth node had its own velocity determined as

$$V_k = \frac{r_k^{m+1} - r_k^m}{\Delta t}$$

where m and Δt are, respectively, the number and value of time step, r_k is the node radius. The time derivative of any function Ψ was approximated as follows:

$$\frac{\partial \Psi}{\partial t} = \frac{\Psi_k^{m+1} - \Psi_k^m}{\Delta t} - V_k \frac{\Psi_{k+1}^{m+1} - \Psi_{k-1}^{m+1}}{r_{k+1}^{m+1} - r_{k-1}^{m+1}}$$

Drop ignition was facilitated by adopting a time-variable activation energy of a rate-controlling gas-phase reaction of fuel decomposition (reaction No. 1 in Table 34.2). A characteristic time of the activation energy relaxation from

very low values (10 kcal/mol) to the reaction-relevant value (50 kcal/mol) was typically 100–200 μs that usually was the order of magnitude less than the drop lifetime. To initiate drop ignition at normal ambient temperature, narrow spikes in gas temperature and combustion products (H_2O and CO_2) concentrations in the close vicinity to the drop surface were initially set.

Before applying the model for predicting the combustion behavior of emulsified-fuel drops, the model was validated against available experimental data for pure-fuel drops. When applying the model to pure-fuel droplet, the parameter η was taken zero.

34.3 RESULTS

34.3.1 Model Validation for Pure-Fuel Drop

Figure 34.1 shows the comparison of predicted $d^2(t)$-curves with experimental data of Jackson *et al.* [22]. In [22], combustion of unsupported fuel drops was observed under conditions of low gravity. Excellent agreement of predictions with the experimental data has been obtained.

Curve in Fig. 34.2 shows the predicted dependence of the combustion constant K of n-heptane drops on the initial drop diameter. In the calculations, the combustion constant is determined as the slope of the $d^2(t)$-curve at the quasi-steady period of drop combustion, i.e.,

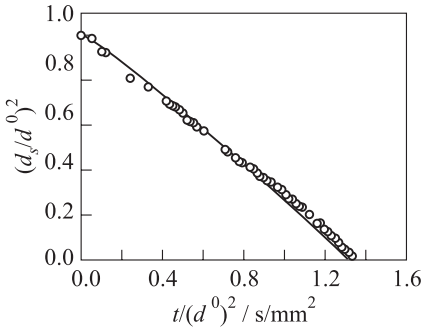

Figure 34.1 Comparison of predicted $d^2(t)$-curves with experimental data of Jackson *et al.* [22] on combustion of unsupported n-heptane drops under normal conditions at low gravity: $d^0 = 0.48$ mm

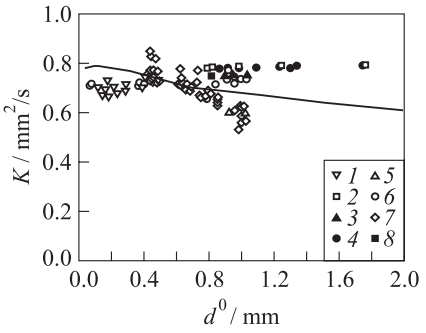

Figure 34.2 Comparison of predicted (curve) and measured (symbols) dependencies of n-heptane combustion constant K on the initial drop diameter: *12* — [23], *2*, *3* — [24], *4* — [25], *5* — [22], *6* — [26], *7* — [27], and *8* — [28]

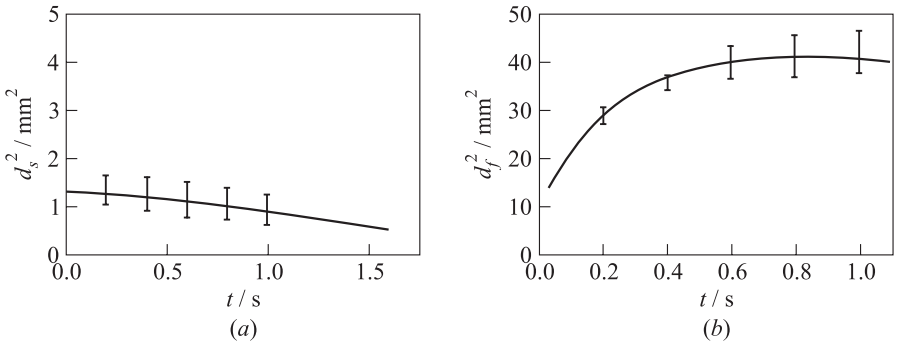

Figure 34.3 Comparison of predicted (curves) and measured (error bars) dependencies of drop (a) and flame (b) diameter for burning n-decane drop under low-gravity conditions. Experimental data by Shaw *et al.* [29]

$$K = -\frac{d(d_s^2)}{dt}$$

Symbols in Fig. 34.2 represent experimental data [22–28] obtained both under microgravity conditions (for relatively large drops with $d_s^0 > 0.4$–0.5 mm) and normal gravity conditions (for relatively small drops $d_s^0 < 0.4$–0.5 mm). In some experimental studies (e.g., [23], the combustion constant was defined as $K = (d_s^0)^2/t_d$, where t_d is the drop lifetime. Clearly, the model correlates fairly good with the measurements within a wide range of initial drop sizes.

For pure n-decane drops, the model provides excellent agreement with low-gravity experimental data by Shaw *et al.* [29] for the evolution of drop (Fig. 34.3a) and flame (Fig. 34.3b) diameter. The latter was defined as the position of temperature maximum.

In the above examples, the maximum gas temperature attained during the drop lifetime varies from 1800 to 2000 K, with higher temperature values related to initially larger drops.

The predicted dynamics and structure of pure-fuel drop flame exhibits several important features. The first one is the existence of a soot shell located between the flame and the drop surface. The second is that the flame, after drop ignition, moves outwards from the drop, but at later stages, it changes the direction of motion (flame "shrinks"). These both features were observed experimentally by Randolph & Law [30], Shaw *et al.* [29], Avedisian *et al.* [31], Hara & Kumagai [32], and Jackson *et al.* [22], and reviewed in the recent paper by Avedisian [33]. Quantitative results are discussed in detail in section 34.3.2.

Figure 34.4 shows the comparison of calculated (curve) and measured (symbols [34]) dependencies of maximum soot volume fraction vs. initial drop diameter for burning n-heptane drops at microgravity conditions. To make the

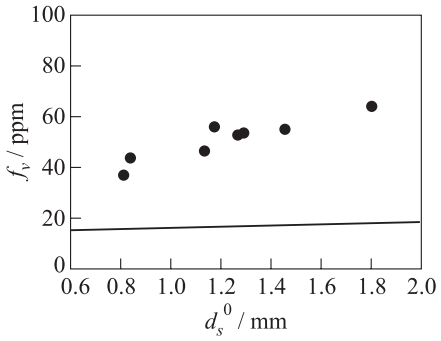

Figure 34.4 Comparison of predicted (solid curve) and measured (symbols) variation of maximum soot volume fraction with initial drop diameter for burning n-heptane drops at normal atmospheric conditions. Experimental data from [34]

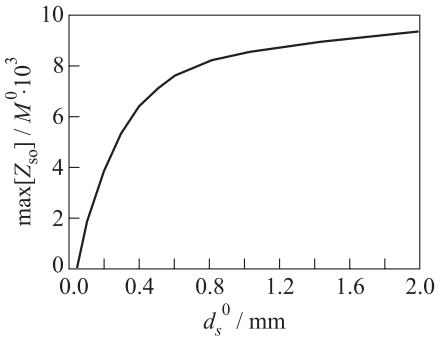

Figure 34.5 Predicted variation of maximum soot yield, $\max[Z_{so}(t)]/M^0$, with the initial drop diameter for combustion of n-heptane drops at ambient pressure and temperature

comparison, the theoretical maximum soot volume fraction, f_v, was determined as follows:

$$f_v = Y_{g,\mathrm{so}}^{\max} \frac{\rho_g}{\rho_{\mathrm{so}}^0}$$

where $Y_{g,\mathrm{so}}^{\max}$ is the maximum (over the entire drop lifetime) local, instantaneous soot mass fraction in the soot shell, ρ_g is the gas density, and ρ_{so}^0 is the density of soot (taken equal to 1850 kg/m^3 [21]). Solid curve corresponds to f_v calculated on the basis of the corresponding local, instantaneous gas density in the soot shell (at elevated temperature). The model correctly reflects the observed trend of slow increase in f_v with the initial droplet diameter. Quantitatively, the values of the predicted soot volume fraction are about 3 times less than the measured values. Taking into account the complexity of actual soot formation processes, the results of comparison can be treated as satisfactory, in particular, in view of very simple model of soot formation adopted in the model.

The model predictions fit experimental observations of Hara & Kumagai [27] who came to a conclusion that soot yield increases with drop size and becomes undetected at small drop diameters (of about 70 μm). Figure 34.5 shows the predicted dependence of maximum soot yield, $\max[Z_{\mathrm{so}}(t)]/M^0$, on the drop diameter for combustion of n-heptane drops at atmospheric pressure and temperature. Soot yield is defined as

$$Z_{\mathrm{so}}(t) = 4\pi \int_{r_s}^{\infty} \rho_{\mathrm{so}}(r,t) r^2 \, dr$$

where $\rho_{so}(r,t) = Y_{g,so}(r,t)\rho_g(r,t)$ and $Y_{g,so}$ is the local instantaneous soot mass fraction. It follows from Fig. 34.5 that at $d_s^0 < 50$–100 μm, the maximum soot yield during drop combustion becomes very small.

With the obtained results on validation of the model for the pure-fuel drop, it is anticipated that predictions for emulsified-fuel drops will be reasonable. Note that the available literature does not contain reliable experimental data on the combustion dynamics of a single emulsion drops.

34.3.2 Comparison of Combustion Performances of Pure-Fuel and Emulsified-Fuel Drops

In this section, as an example of a heavy hydrocarbon fuel, n-tetradecane was used. Water emulsion of n-tetradecane simulates the performance of Aquazole [14]. The main distinctive feature of the emulsion drop gasification is the existence of a relatively long (up to 50% of the drop lifetime) period of drop expansion due to formation of steam bubbles in drop interior. The predicted overheat of steam bubbles attains 100–150 K. Figure 34.6 shows typical predicted surface regression curves for a burning 95% n-tetradecane – 5% water drop (solid curve) and pure n-tetradecane drop (dashed curve) 30 μm in diameter under similar initial conditions at ambient pressure of 1 bar. Contrary to the pure-fuel drop, there is no evidence of the quasi-static d^2-law for the emulsion drop. Approximately for half a lifetime, drop diameter does not decrease below the initial value. Gasification of a single emulsion drop exhibits a fast stage of drop surface regression after passing the maximum in the 'd^2–time' curve. The combustion constant K at this later stage of the drop lifetime is about 2 times higher than that for a pure-fuel drop. Within the present concept of continuous drop evolution, this stage can be conditionally treated as the microexplosion stage.

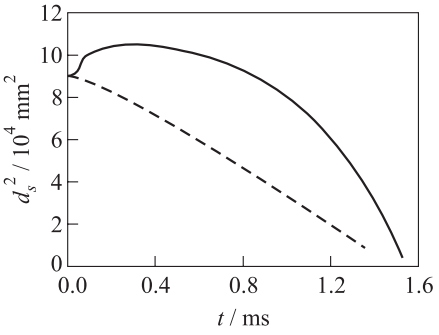

Figure 34.6 Predicted surface regression curves for a burning 95% n-tetradecane – 5% water emulsion drop (solid curve) and pure n-tetradecane drop (dashed curve) under similar initial conditions ($d^0 = 30$ μm, $T^0 = 1200$ K, $p_g = 1$ bar)

The comparison of predicted pure-fuel and emulsified-fuel drop behavior in terms of histories of temperature, mass fractions of fuel, soot, CO, and NO distributions is shown in Figs. 34.7a to 34.7e, respectively. The comparison is made for combustion of pure n-tetradecane drop and 90% n-tetradecane – 10%

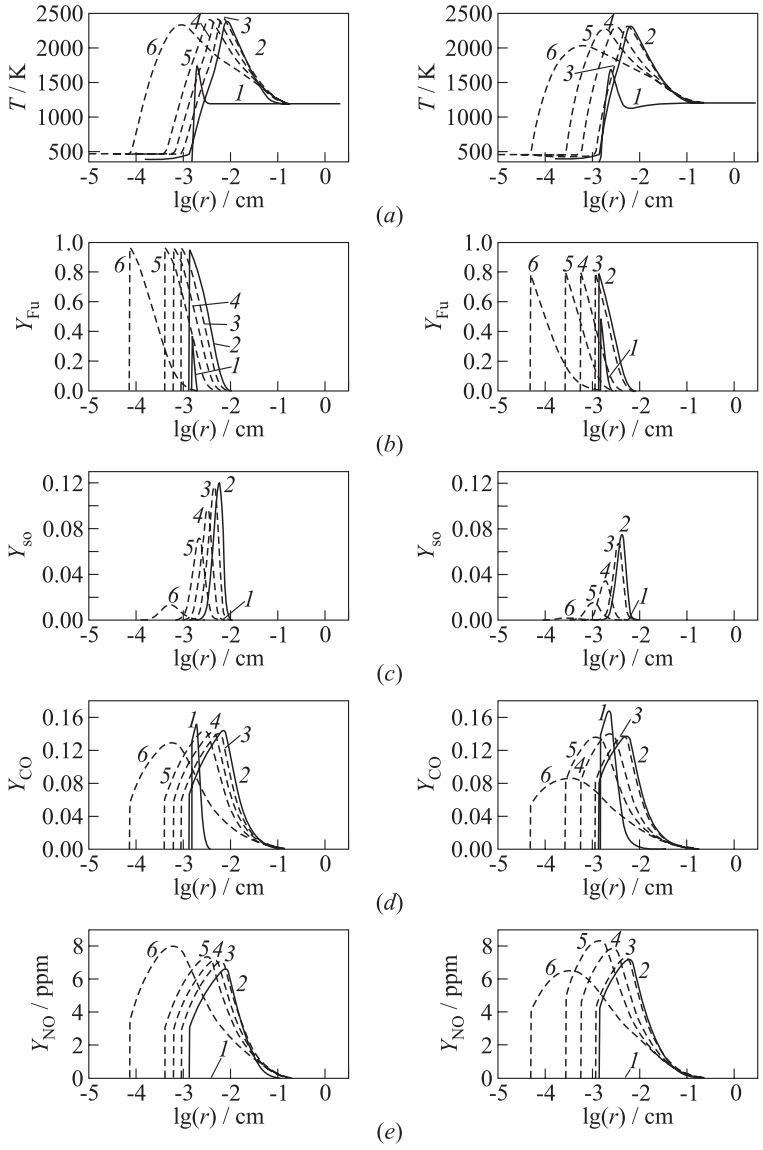

Figure 34.7 Comparison of predicted pure-fuel (left column) and emulsified-fuel (10% H_2O) (right column) drop behavior in terms of histories of temperature (a), mass fractions of fuel (b), soot (c), CO (d), and NO (e) distributions. The comparison is made for combustion of pure n-tetradecane drop and 90% n-tetradecane–10% water emulsion drop under similar initial conditions ($d_s^0 = 30$ μm, $p_g = 1$ bar, $T_g^0 = 1200$ K): *1* — $t = 10^{-4}$ ms, *2* — 0.4, *3* — 0.9, *4* — 1.1, *5* — 1.2, and *6* — $t = 1.27$ ms

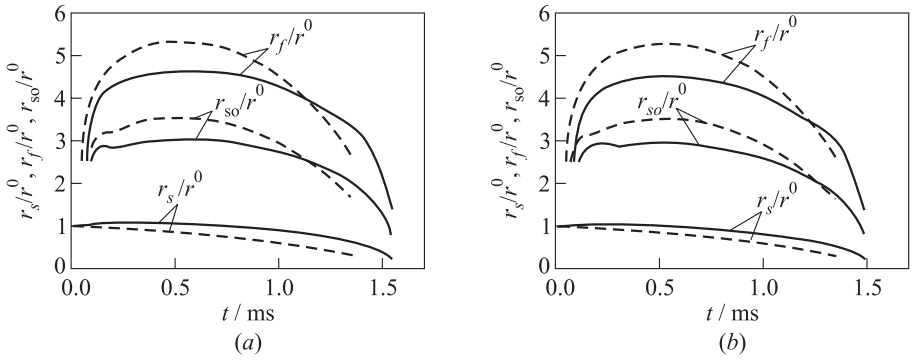

Figure 34.8 Predicted histories of drop radii r_s, flame radii $r_f = r(T_g = T_g^{\max})$ and soot shell radii $r_{so} = r(Y_{g,so} = Y_{g,so}^{\max})$ for pure-fuel (dashed curves) and emulsified-fuel (solid curves) drops. The comparison is made for pure n-tetradecane drop and 90% n-tetradecane – 10% water emulsion drop (a) and pure n-tetradecane drop and 80% n-tetradecane – 20% water emulsion drop (b) under similar initial conditions ($d_s^0 = 30$ μm, $p_g = 1$ bar, $T_g^0 = 1200$ K)

water emulsion drop under similar initial conditions in terms of the drop size and temperature, and the same ambient conditions ($d^0 = 30$ μm, $p_g = 1$ bar, $T_g^0 = 1200$ K). In addition, Fig. 34.8 shows the histories of drop radii r_s, flame radii $r_f = r(T_g = T_g^{\max})$ and soot shell radii $r_{so} = r(Y_{g,so} = Y_{so}^{\max})$ for pure-fuel and emulsified-fuel drops. In Fig. 34.8, the comparison is made for pure n-tetradecane drop, on the one hand, and 90% n-tetradecane – 10% water emulsion drop (Fig. 34.8a) and 80% n-tetradecane – 20% water emulsion drop (Fig. 34.8b), on the other hand, to show the effect of increasing water content, other conditions being similar to those in Fig. 34.7. When considering Figs. 34.7 and 34.8, one can distinguish three stages in the drop history: (1) ignition, (2) outward flame motion, and (3) flame shrinking (shown by dashed curves in Fig. 34.7). The ignition stage is quite similar for pure-fuel and emulsified-fuel drops. At the second stage, the emulsion-drop flame displaces to a shorter distance from the drop surface as compared to the pure-fuel drop flame. Moreover, the maximum temperature in the emulsion drop flame is less due to the effect of water. The third stage is somewhat more pronounced for the emulsion drop.

These peculiarities are explained by the fact that addition of a volatile component (water) results in diminishing the fuel vapor partial pressure at the drop surface and the amount of fuel vapor accumulated between the drop surface and the flame. It is clearly demonstrated in Fig. 34.7b. As a result of this, and due to a more pronounced flame shrinking with the emulsion drop, the amount of soot formed is significantly less for the emulsion drop (Fig. 34.7c). As it follows from Figs. 34.7c and 34.8, the burning process of a drop is accompanied with the

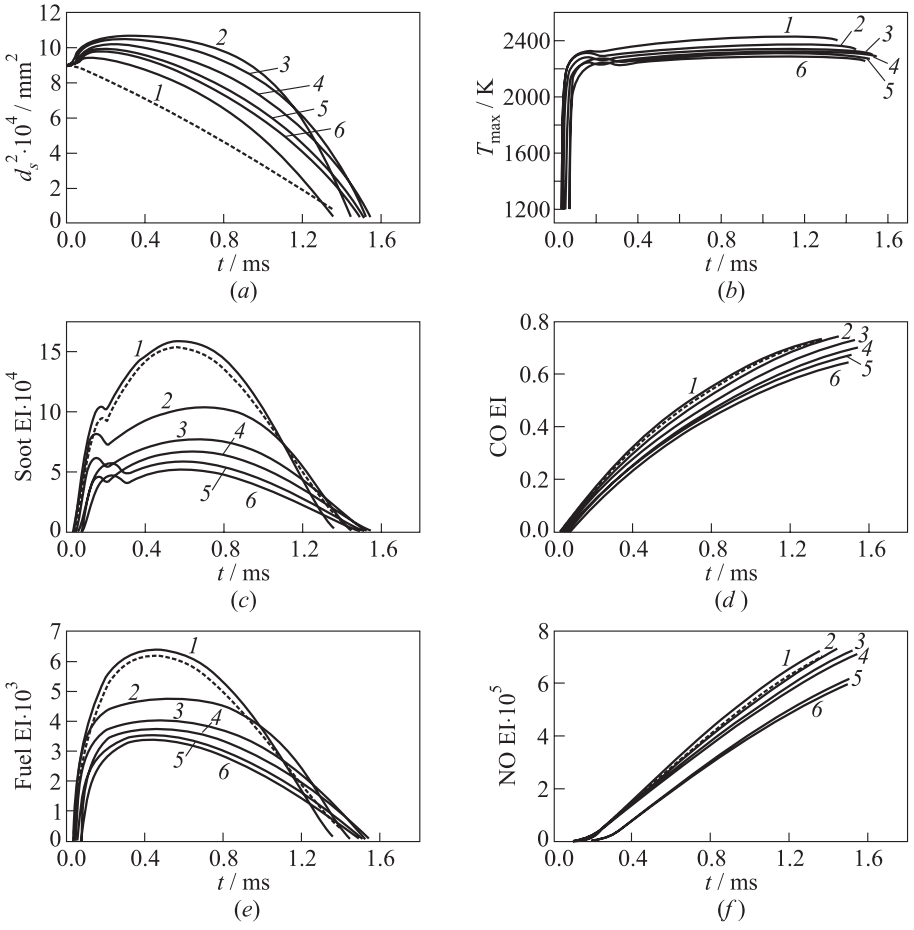

Figure 34.9 Predicted histories of squared drop diameter (a), maximum combustion temperature $T_g^{\max}$ (b), and EIs of soot (c), CO (d), unreacted fuel (e), and NO (f) for burning n-tetradecane–water emulsion drop with different water loading ratio (from 0% to 20% wt.) at fixed initial conditions ($d_s^0 = 30$ μm, $p_g = 1$ bar, $T_g^0 = 1200$ K). Dashed lines refer to 0%; *1* — 0.1%; *2* — 1%; *3* — 5%; *4* — 10%; *5* — 15%; and *6* — 20%

formation of a spherical soot shell inside the flame. The shell initially forms close to the drop surface. After some time, the shell maintains a relatively constant thickness. The mass fraction of soot in this shell structure rapidly increases as combustion proceeds until near the end of burning when the flame begins to shrink. The shrinking flame approaches the soot shell, resulting in soot oxidation before flame extinguishing. Similar to the amount of soot, the amounts of

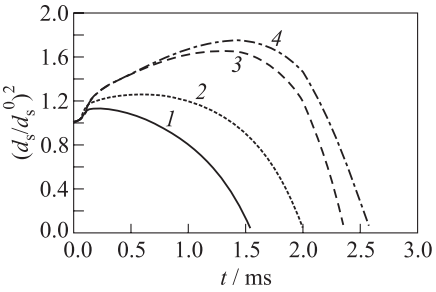

p, bar	$T_{\max}$, K	EI NO·10^6
1	2323	72
2	2207	68
5	2139	67
20	1866	21

Figure 34.10 Predicted effect of ambient pressure p_g^0 on the d^2–t-curves for the burning 90% n-tetradecane – 10% water emulsion drop of 30-micrometer initial diameter at ambient temperature of 1200 K: *1* — $p_g^0 = 1$ atm, *2* — 2, *3* — 5, and *4* — $p_g^0 = 20$ atm. Table shows the predicted maximum combustion temperatures and NO emission index

CO and NO around the emulsified-fuel drop are also less as compared to the pure-fuel drop towards the end of lifetime (see Figs. 34.7*d* and 34.7*e*).

It is instructive to compare emission indices for combustion of pure-fuel and emulsion drops. The emission index (EI) for the jth species is defined as the ratio of the total mass of this species in the gas phase to the initial drop mass, i.e.,

$$(\mathrm{EI})_j = \frac{4\pi \int\limits_{r_s}^{\infty} \rho_{gj}\, r^2\, dr}{M^0}$$

where ρ_{gj} is the partial density of the jth species in the gas phase. Figure 34.9 shows the predicted emission indices of soot (Fig. 34.9*c*), CO (Fig. 34.9*d*), unreacted fuel (Fig. 34.9*e*), and NO (Fig. 34.9*f*) for the n-tetradecane drop with different amount of water (from 0% to 20%). To make the comparison more informative, Figs. 34.9*a* and 34.9*b* present the corresponding 'd^2–time' curves and the curves of the maximum combustion temperature $T_g^{\max}(t)$. The initial temperature "bulbs" in Fig. 34.9*b* correspond to the ignition stage.

It follows from Fig. 34.9 that addition of water in the amount higher than 1% results in a monotonous decrease in EI of soot, CO, unreacted fuel, and NO. At small water addition (less than about 1%), a slight increase in the EIs has been predicted. With the increase in water content from 0% to 20%, the drop lifetime varies by less than 10%. (Fig. 34.9*a*) and maximum combustion temperature decreases by about 10%.

Figure 34.10 shows the effect of initial pressure p^0 (from 1 to 20 bar) on the d^2–t-curves, together with the predicted data on maximum combustion temperatures and NO emission indices at various pressures. Clearly with increasing initial pressure the conditional microexplosion stage in drop evolution becomes more pronounced.

34.4 CONCLUDING REMARKS

The paper describes the mathematical model of emulsified-fuel drop combustion and the results of its implementation. The model has been validated against available experimental data for combustion of pure-fuel drops under low-gravity (relatively large drops) and normal gravity (small drops) atmospheric conditions. It has been shown that addition of water to a hydrocarbon fuel allows one to control drop combustion and emission performances. Of particular importance are the following findings:

(1) The main distinctive feature of the emulsion drop gasification is the existence of a relatively long period of drop expansion due to formation of steam bubbles in drop interior. Gasification of a single emulsion drop exhibits a fast stage of drop surface regression after passing the maximum in the 'd^2–time' curve;

(2) The burning process of pure-fuel and emulsified-fuel drops is accompanied with the formation of a spherical soot shell between the drop surface and flame;

(3) Addition of water to hydrocarbon fuel results in diminishing the fuel vapor partial pressure at the drop surface and the amount of fuel vapor accumulated between the drop surface and flame. As a result of this, and due to a more pronounced flame shrinking with the emulsion drop, the amount of soot formed is significantly less for the emulsion drop;

(4) Similar to the amount of soot, the amounts of CO and NO around the emulsified-fuel drop are also less as compared to the pure-fuel drop;

(5) Addition of water to hydrocarbon fuel in the amount higher than 1% (wt.) results in a monotonous decrease in emission indices of soot, CO, unreacted fuel, and NO. With the increase in water content from 0% to 20%, the droplet lifetime varies by less than 10% and the maximum combustion temperature decreases by about 10%.

These findings are in qualitative agreement with experimental data on emulsified fuel (Aquazol) combustion in Direct Injection Diesel engines. It has been reported by Desantes *et al.* [14] that the use of emulsified fuel resulted in a considerable reduction of smoke as well as some reduction in CO and NO emission in engine exhaust gases.

REFERENCES

1. Cornet, I., and W. E. Nero. 1955. Emulsified fuels in compression ignition engines. *Ind. Eng. Chem.* 47(10):2133.
2. Ivanov, V. M. 1962. *Fuel emulsions*. Moscow: USSR Acad. Sci. Publ.

3. Lebedev, O.N. 1978. Some peculiarities of combustion of fuel–water emulsions in Diesel engines. *Combustion Explosion Shock Waves* 14(2):142.
4. Morrone, T., R. Lippman, and D. Wright. 1979. *2nd Symposium on Water-in-Fuel Emulsions in Combustion Proceedings*. U.S. Department of Transportation. 29.
5. Lasheras, J.C., A.C. Fernandez-Pello, and F.L. Dryer. 1980. *Combustion Science Technology* 22:195–209.
6. Law, C.K., C.H. Lee, and N. Srinivasan. 1980. *Combustion Flame* 37:125.
7. Gollahalli, S.R., M.L. Rasmussen, and S.J. Moussavi. 1981. Combustion of drops and sprays of No. 2 Diesel oil and its emulsions with water. *18th Symposium (International) on Combustion Proceedings*. Pittsburgh, PA: The Combustion Institute. 349–59.
8. Lasheras, J.-C., A.C. Fernandez-Pello, and F.L. Dryer. 1981. On the disruptive burning of free droplets of alcohol/n-paraffin solutions and emulsions. *18th Symposium (International) on Combustion Proceedings*. Pittsburgh, PA: The Combustion Institute. 293–305.
9. Wang, C.H., X.Q. Liu, and C.K. Law. 1984. Combustion and microexplosion of freely falling multicomponent droplets. *Combustion Flame* 56:175–97.
10. Prostov, V.N., A.V. Yakovlev, and V.A. Gladkikh. 1986. Ignition of fuel–water emulsions. *Combustion Explosion Shock Waves* 14(5):9–14.
11. Tsue, M., H. Yamasaki, T. Kadota, D. Segawa, and M. Kono. 1998. Effect of gravity on onset of microexplosion for an oil-in-water emulsion droplet. *27th Symposium (International) on Combustion Proceedings*. Pittsburgh, PA: The Combustion Institute. 2587–93.
12. Law, C.K. 1977. A model for the combustion of oil/water emulsion droplets. *Combustion Science Technology* 17:29–38.
13. Shusser, M., and D. Weihs. 1999. Stability of explosive boiling of fuel droplets. *Symposium (International) on Air-Breathing Engines*. Florence, Italy. ISABE Paper 99-7279.
14. Desantes, J.M., J. Arregle, S. Ruitz, A. Delage, P. Schmelzle, and O. Esmilaire. 1999. Characterization of the injection-combustion process in a common-rail D.I. Diesel engine running with fuel–water emulsion. *EAEC Proceedings*. Barselona.
15. Delhaye, J.M., M. Giot, and M.L. Reithmuller, eds. 1981. *Thermohydraulics of two-phase systems for industrial design and nuclear engineering*. Washington, DC: Hemisphere Publ. Co.
16. Reid, R.C., J.M. Prausnitz, and T.K. Sherwood. 1977. *The properties of gases and liquids*. 3rd ed. New York: McGraw Hill Book Co.
17. Kuznetsov, N.M. 1982. Equation of state and the phase equilibrium curve for liquid–vapor systems. *Soviet Doklady* 266(3):613–16.
18. Basevich, V.Ya., A.A. Belyaev, and S.M. Frolov. 1998. Global kinetic mechanisms for calculating turbulent reactive flows. Part I. The basic chemical heat release process. *Chemical Physics Reports* 17(9):1747–822.
19. Basevich, V.Ya., A.A. Belyaev, and S.M. Frolov. 1998. Global kinetic mechanisms for calculating turbulent reactive flows. Part II. Formation of nitrogen oxide. *Chemical Physics Reports* 17(10):1895–908.

20. Evlampiev, A.V., S.M. Frolov, V.Ya. Basevich, and A.A. Belyaev. 2001. Global kinetic mechanisms for calculating turbulent reactive flows. Part IV. Diffusion combustion. *Chemical Physics Reports* 20(11):21.
21. Xu, F., K.-C. Lin, and G.M. Faeth. 1998. Soot formation in laminar premixed methane/oxygen flames at atmospheric pressure. *Combustion Flame* 115:195–209.
22. Jackson, G.S., C.T. Avedisian, and J.C. Yang. 1992. Observations of soot during droplet combustion at low gravity: Heptane and heptane/monochloroalkane mixtures. *Int. J. Heat Mass Transfer* 35(8):2017–33.
23. Monaghan, M.T., R.G. Siddall, and M.W. Thring. 1968. The influence of initial diameter on the combustion of single drops of liquid fuel. *Combustion Flame* 12:45–53.
24. Kumagai, S., T. Sakai, and S. Okajima. 1971. Combustion of free fuel droplets in a freely falling chamber. *13th Symposium (International) on Combustion Proceedings*. Pittsburgh, PA: The Combustion Institute. 779–85.
25. Okajima, S., and S. Kumagai. 1975. Further investigations of combustion of free droplets in a freely falling chamber including moving droplets. *15th Symposium (International) on Combustion Proceedings*. Pittsburgh, PA: The Combustion Institute. 401–7.
26. Hara, H., and S. Kumagai. 1994. The effect of initial diameter of free droplet combustion with spherical flame. *25th Symposium (International) on Combustion Proceedings*. Pittsburgh, PA: The Combustion Institute. 423–30.
27. Jackson, G.S., and C.T. Avedisian. 1994. The effect of initial diameter in spherically symmetric droplet combustion of sooting fuels. *Proc. Royal Society London A* 446:255–76.
28. Mikami, M., H. Kato, J. Sato, and M. Kono. 1994. Interactive combustion of two droplets in microgravity. *25th Symposium (International) on Combustion Proceedings*. Pittsburgh, PA: The Combustion Institute. 431–38.
29. Shaw, B.D., F.L. Dryer, and F.A. Williams. 1988. Sooting and disruption in spherically symmetrical combustion of decane droplets in air. *Acta Astronautica* 17(11/12):1195–202.
30. Randolph, A.L., and C.K. Law. 1986. Influence of physical mechanisms on soot formation and destruction in droplet burning. *Combustion Flame* 64:267–84.
31. Avedisian, C.T., J.C. Yang, and C.H. Wang. 1988. On low-gravity droplet combustion. *Proc. Royal Society London A* 420:183–200.
32. Hara, H., and S. Kumagai. 1990. *23rd Symposium (International) on Combustion Proceedings*. Pittsburgh, PA: The Combustion Institute. 1605–10.
33. Avedisian, C.T. 2000. Recent advances in soot formation from spherical droplet flames at atmospheric pressure. *J. Propulsion Power* 16(4):628–35.
34. Lee, O.L., S.L. Manzello, and M.Y. Choi. 1998. The effects of initial diameter on sooting and burning behavior of isolated droplets under microgravity conditions. *Combustion Science Technology* 132:139–56.